13th International Symposium on Particle Image Velocimetry – ISPIV 2019
Munich, Germany, July 22-24, 2019

Conditional averages of large scale motions through synchronous PIV and surface shear stress measurements

Rommel J. Pabon[1], Lawrence Ukeiley[1*], David Mills[2], Mark Sheplak[1,2]

[1] University of Florida, Mechanical and Aerospace Engineering, Gainesville, FL USA

[2] Interdisciplinary Consulting Corp, Gainesville, FL, USA

[*] ukeiley@ufl.edu

Abstract

Synchronous stereo particle image velocimetry (PIV) and fluctuating wall shear stress measurements were performed in a moderate Reynolds number zero pressure gradient turbulent boundary layer. Multiple, discrete PIV planes allow for a reconstruction of the wall shear stress-streamwise velocity cross correlation in a volume around the sensor. The velocity field is averaged on imposed conditions of the wall shear stress to identify large scale motions during these conditions. A simple condition based on large scale dynamics is introduced to identify periodic patterns of the velocity field associated with wall-distance scaling. This study represents a novel application of microelectromechanical systems floating element wall shear stress sensor types simultaneously with PIV, and addresses experimental procedures to prevent degradation and signal corruption caused by both seeded flow and laser radiation.

1 Introduction

With recent advances in microelectromechanical systems (MEMS) manufacturing, a variety of sensor types have been introduced into the fluid experimentalist's toolbox that help facilitate the understanding of flow structures. These not only assist in detailed studies paired with simulations for validation purposes, but are required for very large Reynolds number experiments where traditional apparatus fail to resolve required scales. Therefore, the need for time resolved, accurate measurement of the fluctuating wall shear stress, τ'_w, is expected to increase as flow Reynolds numbers increase. MEMS flush mounted wall shear stress sensors enable a direct, non intrusive sensing method that captures relevant flow scales without imposing restrictive assumptions on the flow (Naughton and Sheplak (2002)). These sensors are expected to play an important role in revealing the organized motions in the velocity field that have the greatest impact in the wall shear stress. However, their ability to withstand the experimental conditions of particle image velocimetry (PIV) has still not been studied. This includes the undesirable sensitivity to incident fluence and associated electromagnetic interference with generating the laser pulse as well as damping or damage when a floating element sensor is exposed to a seeded environment.

The importance of wall measurements in this work is to capture energetic motions through the use of conditional sampling and averaging. These techniques have identified phenomena critical to the life cycle of turbulence in a turbulent boundary layer, and are still used to propose structures that involve the coherent alignment of smaller structures (Kovasznay et al. (1970); Wallace et al. (1972); Zhou et al. (1999)). Blackwelder and Kovasznay (1972) introduced the variable interval time average (VITA) as a detection criteria for turbulence in a localized spatio-temporal region. The VITA of a fluctuating quantity $q'(t)$ can be defined as

$$\mathrm{VITA}(q') = \hat{q}(t,T) = \frac{1}{T}\int_{t-T/2}^{t+T/2} q'(s)ds, \tag{1}$$

which serves as a local averaging technique with arbitrary averaging time T, which should be of the order of the relevant flow time scale. In addition, Blackwelder and Kaplan (1976) added a measure of the local

turbulent energy by applying the VITA to the square of the velocity, called the VARVITA of the signal,

$$\text{VARVITA}(q') = \widehat{var}(t,T) = \widehat{u^2}(t,T) - [\hat{u}(t,T)]^2 . \tag{2}$$

where detection criteria can be defined as a threshold when the VARVITA exceeds a chosen constant multiplier of the global variance. These techniques, and others such as number of zero crossings, are principally statistics based, and do not use dynamics in previous measurements, for example, as condition. Dynamic changes in the shear stress can be introduced to monitor bursting-sweeping incidents or large scale changes of shear direction. However, the high turbulence of the wall shear stress occludes information directly from differential measurements as being a result of high turbulence events. Therefore, a technique to isolate scales of interest needs to be introduced. In this work, a variety of conditional sampling techniques will be applied to identify aspects of large scale motions utilizing the synchronous measurement of velocity through PIV and fluctuating wall shear stress through MEMS floating element wall shear stress sensors.

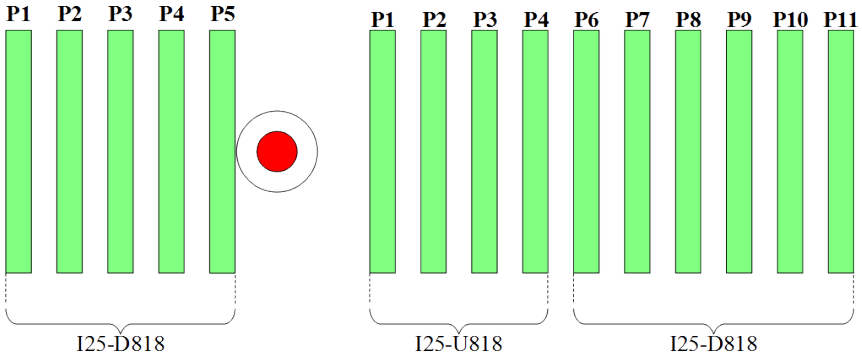

Figure 1: Schematic of PIV measurement planes (in green) relative to static sensor location (in red), with nominal spacing between planes (except for near sensor) of 8 mm ($\approx 0.3\delta$) and plane thickness of 3.8 mm.

2 Experimental Methods

2.1 Facility

All experiments were performed in the Engineering Laboratory Design (ELD) 407B circulating wind tunnel at the University of Florida. The ELD tunnel uses a heat exchanger mounted alongside a flow conditioning section, along with a set point controller to regulate incoming chilled water flow so that air temperature can be controlled to within $\pm$ 1°C. Downstream of this section and a 25:4 area contraction, the experimental test section was mounted with dimensions of 0.61 m $\times$ 0.61 m $\times$ 2.44 m, and a velocity range up to 90 m/s, with optical access to the test section interior provided by acrylic windows on all four sides. Further details of the experimental configuration used for this study can be found in Pabon (2018).

A flat plate model was installed in the test section to create a turbulent boundary layer on the top surface. The leading edge used the optimized profile of Hanson et al. (2012) to reduce the length of the non-zero pressure gradient region. An aluminum trailing edge flap is used to control the circulation around the flat plate by rotation around a supporting hinge, in practice, along with a streamwise row of static pressure taps, a linear pressure gradient can be imposed on the top surface. For a given run speed, a trailing edge flap angle is interpolated from a library of previous measurements that results in a zero pressure gradient across the measurement surface. The measurement windows of the flat plate model allow the shear stress sensor to be placed 1.41 m from the leading edge, allowing for both upstream and downstream viewing from cameras. Along with sandpaper roughness for tripping near the leading edge, at a nominal run speed of 25 m/s, Re_θ for the measurement planes was between 4200 and 4400. For further details on the construction, design, and implementation of the zero pressure gradient condition, the reader is directed to Pabon et al. (2018), where hot-wire measurements were performed in the same experimental setup.

2.2 Particle Image Velocimetry

Stereo particle image velocimetry was utilized to capture non-time resolved, two-dimensional, three-component velocity fields at a series of measurement planes relative to the shear stress sensor. The illumination source was a Litron Nano L 135-15 Nd:YAG laser outputting 532 nm wavelength light, with a maximum output and double-pulse repetition rate of 135 mJ and 15 Hz, respectively. A focusing and cylindrical lens optical setup allowed a light sheet thickness approximately 3.8 mm thick. While on the higher end of recommended thicknesses (Raffel et al. (2007)), this experimental choice allowed for larger pulse time separations, thus allowing higher particle displacements in the in-plane directions. Two LaVision Imager sCMOS cameras with a sensor size of 2560 $\times$ 2160 pixels, a maximum frame rate of 50 Hz, and 16-bit digital output were used with a stereoscopic angle of 68°, with the cameras on either spanwise side of the wind tunnel. This angle helps improve robustness to the out-of-plane velocity gradients and other factors during calibration LaVision (2016). The cameras were equipped with 200 mm lenses, and for certain positions, polarizing filters to reduce the specular reflection of the laser plane off of the acrylic plate.

A LaVision type 11 calibration plate was utilized along with external LED lighting to carry out the stereo calibration procedure, and to focus the image plane as close as possible to the laser plane. A pinhole model is utilized to ensure approximate agreement between the calculation and the physical setup, as well as to ensure the edges of the image (areas typically without calibration target spots), especially near the wall, will be correctly calibrated. For a given plane, a preliminary image set of 200 images is used for the self-calibration step to improve the calculation of the location of the image plane relative to the laser plane. Disparity vectors are minimized until average disparity is below 0.3 px for a new triangulated plane as close as possible to the light sheet center. A Gaussian mean with filter length of 7 image pairs is subtracted over the images to eliminate background artifacts from the data. A minor pre-processing step was used after this to normalize particle intensities and backgrounds, primarily to correct minor differences in the laser intensity along the plane. The spectral cross correlation step is implemented on interrogation windows of ratio 2:1 (spanwise:wall-normal). Two initial passes are performed to refine the windows with 50% overlap, and the final two passes utilized adaptive windows with one-quarter the initial area, resulting in the final vector grid resolution. Between passes, only vectors with peak-to-peak ratios (*PPR*) worse than 1.1 are removed, along with a minor universal outlier detection median filter (Nogueira et al. (1997); Westerweel et al. (2005)). High-accuracy mode with B-spline-6 reconstruction is utilized in the final pass.

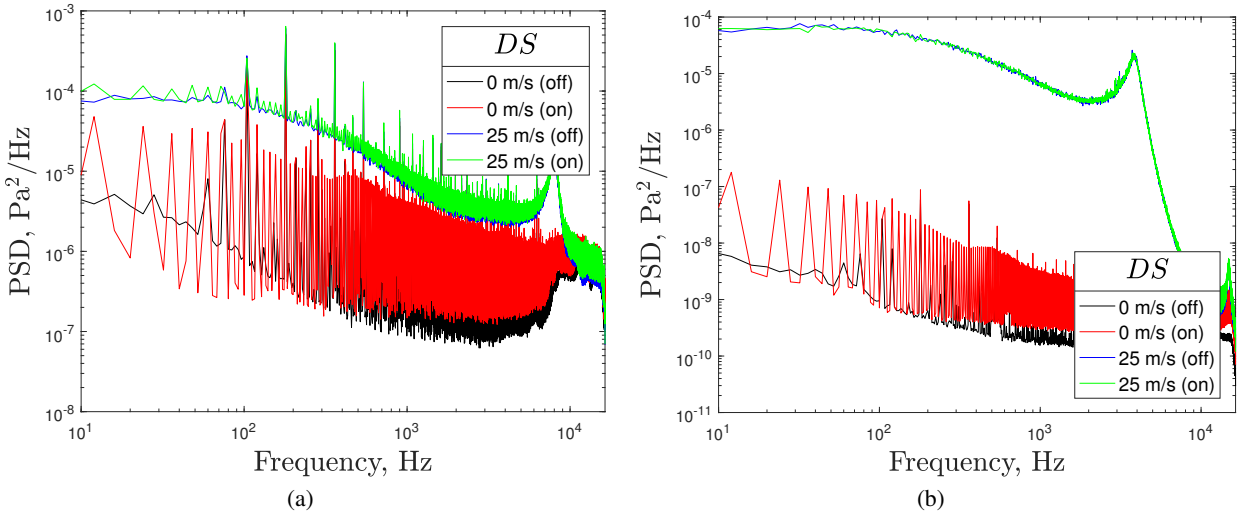

Figure 2: Power spectral density of CSSS at 25 m/s compared to noise floor (0 m/s) with (on) and without (off) simultaneous PIV laser firing at a distance of 7 mm. A) CS-A05 sensor with SNR = 4 dB, and B) CS-D100 sensor with SNR = 33 dB, each at 1 kHz.

The major post-processing steps after vectors are calculated increases the *PPR* tolerance to 1.25, with the same tolerance in median filter, to iteratively find preferred peaks. If a grid point failed all these steps, spatial interpolation was introduced, but there is no smoothing introduced in any pass. Interpolation was found to occur in approximately 1% of a given snapshot, with 90% of these interpolated points occurring at or just above the physical wall. Thus, masking the first calculated row above the wall drastically cut down

spurious vectors, resulting in the closest wall normal position to the wall being near 320 μm. After the stereo and self calibration steps, the rms fit error was calculated at 1.02 px, the scale factor was 63 px/mm, and the vector grid resolution was 254 μm.

Eleven separate measurement planes are utilized, where illumination planes were wall-normal, spanwise oriented, with a series of such planes at different relative streamwise locations relative to the sensor. This is seen in a schematic in Fig. 1, spanning a streamwise distance of about 6δ and a total of 96000 image pairs. Most planes were composed of 8000 image pairs, with the first plane consisting of 16000 image pairs to verify statistical convergence. A nominal spacing between planes of 8 mm, approximately 2 laser plane thicknesses is used, except for directly on top of the sensor, and just downstream. While direct incident laser radiation was avoided due to data contamination to be discussed in a later section, the experimental setup did not allow for calibration just downstream of a sensor due to placement of the calibration plate, with the sensor needing to be mounted during calibration to avoid movement of cameras and windows.

2.3 Capacitive Shear Stress Sensor

Two IC2 DirectShear CS-D100 MEMS floating element differential capacitive shear stress sensors (CSSS) were used in this study, identified as I25-D818 and I25-U818. Their floating element sizes are 2 mm $\times$ 0.4 mm ($L^+ \times W^+ \approx 126 \times 25$), with the major axis aligned in the streamwise direction. They have bandwidths of 2.5 kHz ($f^+ \approx 0.2$), sensitivities of 29 mV/Pa, and height perturbations from manufacturing and assembly of approximately 25 μm ($h^+ \approx 1.$), allowing a flushness approximation for the sensor die. They are each powered by an external sensor control unit with battery operation mode to attenuate power line noise. The reader is directed to Mills et al. (2018) and Mills et al. (2017) for a comprehensive guide to the manufacturing processes behind the sensor system, as well as recent developments improving the sensor, electronics, and control unit for aerodynamic measurements.

While higher bandwidth sensors were considered with the goal of resolving the smallest relevant flow scales, the current sensors were chosen because they provided sufficient signal sensitivity to overcome response to the laser pulse. A comparison between a CS-A05 sensor, with a bandwidth of 5 kHz, and the CS-D100 used in this study is presented in Fig. 2 when presented with laser radiation at a distance of 7 mm, with the signal-to-noise ratio of the CS-D100 being 33 dB. This was determined to be sufficient to continue experiments, although reflective coating and other electronic changes to avoid such contamination is suggested for future sensor designs.

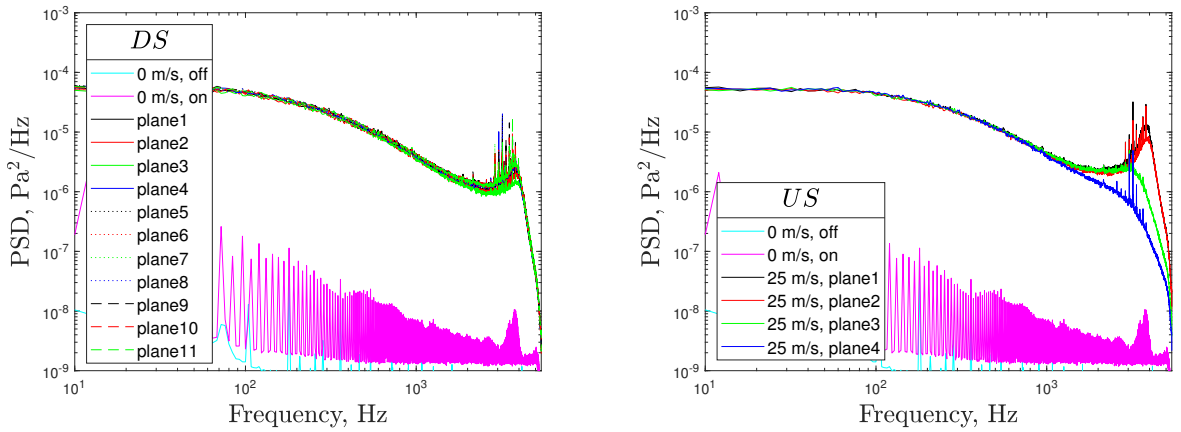

Figure 3: Power spectral density of CSSS measurements over full range of measurements, verifying laser degradation over time, A) for I25-D818 sensor, which lasted for all eleven PIV planes, and B) for I25-U818 sensor, which failed for undetermined reasons, most likely due to PIV seeding, after the fourth PIV plane.

The CS-D100 was not rated for use in a seeded environment as would be required for PIV, and preliminary experiments suggested that long-term sensor degradation was possible. A procedure was implemented to minimize the opportunities for seed to become trapped under the floating element and between the comb fingers. First, the CSSS were removed with the tunnel still running at low speeds ($<$ 5 m/s), to prevent the

density difference from allowing the seed to deposit on the top surface of the flat plate, and thus the sensor. For future work, a similar experiment is recommended to use the measurement surface on the bottom side of the plate, so that seed is less likely to settle on the die head. In addition, during removal, a tunnel window was opened to allow entrainment of unseeded air in the room and further minimize number density in the test section. Second, the sensor was physically transported to a separate room without seed present for storage. Finally, sensor checks before and after runs were implemented to track and verify sensor functionality. However, sensor degradation was not totally avoided, and the second sensor, I25-U818, failed after the fourth plane. A comparison of the power spectral density between the two sensors is presented in Fig. 3, with a degradation around the resonant peak visible between planes for the -U818 sensor, but not for the -D818 sensor. This degradation did not affect the measurements, due to the low-pass filter removing the sensor response past the bandpass frequency, as well as the magnitude response of the sensor at each plane being very consistent in the passband. The degradation near the resonant peak suggests seed related damping, and finally failure, and after microscopic investigation, the floating element is seen to be clamped to one set of sensor electrodes. The fact that each sensor was given the same treatment implies a substantial risk to CSSS use in seeded flow unless changes are made to the sensor design. After the failure of the -U818 sensor, experiments were repeated using only the -D818 sensor, with an increased number of required planes to capture the desired streamwise field of view. The compound reconstruction of the PIV planes onto a single, artificial 'global' sensor is seen in Fig. 1, where the planes relative to each sensor used are displayed. The sensors were mounted 38.1 mm apart ($\approx 1.75\delta$), differences in energy due to downstream distance (i.e. Re_θ of 4250 vs 4300) were considered negligible for the reconstruction.

3 Results and Discussions

The wall shear stress is captured synchronously with the velocity, but at different sampling speeds, 10.8 kHz and 12 Hz, respectively, each triggered to begin on the first laser pulse. The wall shear stress signal is low pass filtered at its +3 dB cutoff bandwidth of 2.5 kHz. Since temporal information pre- and post- laser pulse is required, the data from the first and last laser pulse and resulting wall shear stress information is discarded.

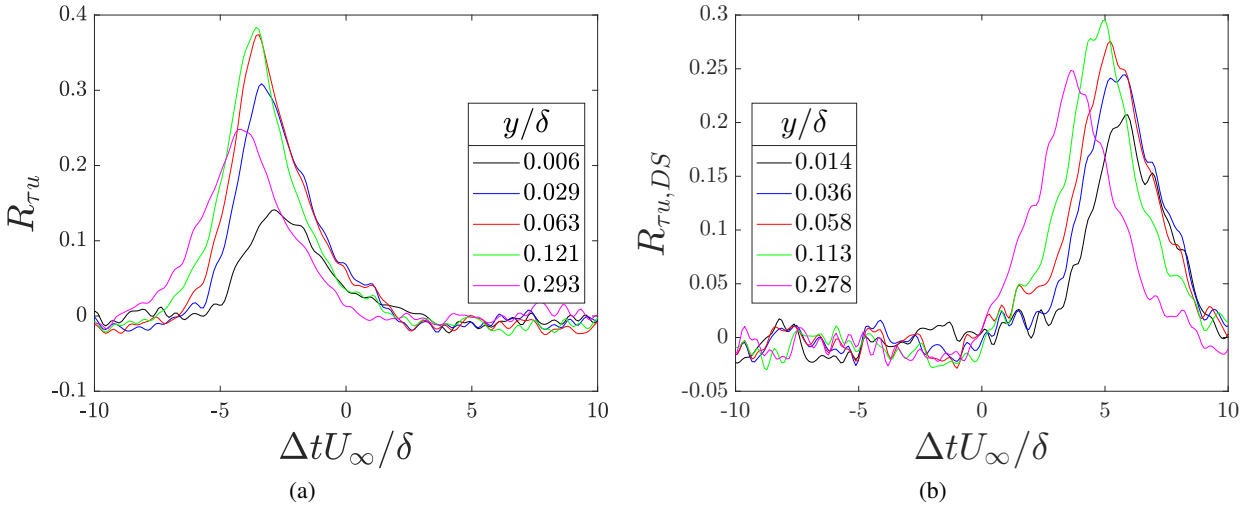

Figure 4: $R_{\tau u}$ vs. non-dimensional time delay for select wall normal positions along the spanwise centerline for PIV planes with streamwise location $x_p/\delta =$ a) -1.82, and b) 3.95.

3.1 Cross correlation

Typically, the temporal cross correlation coefficient between wall shear stress and streamwise velocity, $R_{\tau u}$, would be calculated in spectral space for the popularity and efficiency of FFT algorithms, but this is not possible in the current study with the PIV sampling rate being much lower than the wall shear stress sampling rate. Instead, an average over a certain temporal separation window is performed, assuming that an

instantaneous PIV sample retains its value between each sample for necessity of the averaging process. The window used is approximately $\Delta t U_\infty/\delta = 20$ to allow a return to zero correlation at extreme time lags for the extremes of the PIV planes. The result is displayed in Fig. 4 for the most upstream and downstream plane, respectively, with respect to the sensor located at $x_p = 0$. Convection of the correlation is observed, as well as a decorrelation with distance from the sensor. The approximate noise value (rms of the correlation at 'extreme' time lags) of $R_{\tau u}$ is approximately 0.02. The primary source of noise is first, the cross correlation procedure which reduces the number of averages compared to spectral methods, for example, and second, the sPIV algorithm itself. However, the relatively high correlation coefficient values (≈ 0.5), compared favorably to previous HWA experimental values (Pabon et al. (2018)), suggesting estimation methods using PIV based on correlations are achievable.

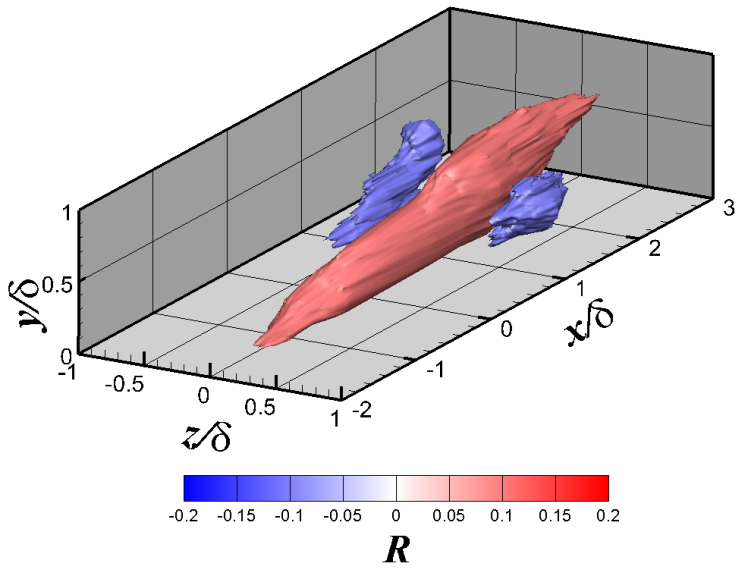

Figure 5: Volumetric reconstruction of isosurfaces of $R_{\tau u}(t = 0)$ calculated in each PIV data plane, $R_{\tau u} = 0.1$ in red and $R_{\tau u} = -0.1$ in blue.

At each measurement plane, $R_{\tau u}(\delta t = 0)$, the zero time lag cross correlation, is presented in Fig. 5, using a volumetric reconstruction, interpolating between planes, and an isosurface threshold of $R_{\tau u} > \pm 0.1$ for red and blue surfaces, respectively. The principal positively correlated region is approximately $4\delta \times 0.5\delta \times 0.5\delta$, with smaller negatively correlated regions flanking on either side. While the data could be averaged along the z-axis to improve the statistical representation, the resulting asymmetries qualitatively show limits of the experimental setup in terms of noise, error, or any actual asymmetries present.

3.2 Conditional Averages

To describe an average picture of the velocity field during intense events of the wall shear stress, conditional averaging is applied. This procedure presents a qualitative view of the flow field on average during desired wall shear stress events. This allows a comparison of the effect of threshold level as well as symmetry of threshold during locally positive vs negative shear events around the global mean. Conditions described in Pabon et al. (2018) are used here, to calculate the mean streamwise velocity conditioned on positive shear fluctuation, $\widetilde{U}_h$, and on negative shear fluctuation, $\widetilde{U}_l$, such that

$$\widetilde{U}_h(x,y,z) = \langle u(x,y,z,t) | \tau'_w(x = y = z = 0,t) > 0 \rangle, \tag{3}$$

$$\widetilde{U}_l(x,y,z) = \langle u(z,y,z,t) | \tau'_w(x = y = z = 0,t) < 0 \rangle, \tag{4}$$

Fig. 6 shows isosurfaces of the difference between these conditionally averaged flow fields and the global mean velocity field, $\Delta U_h^+(x,y,z) = (\widetilde{U}_h - U(x,y,z))/u_\tau$ and $\Delta U_l^+(x,y,z) = (\widetilde{U}_h - U(x,y,z))/u_\tau$, respectively. The red and blue isosurfaces represent $\Delta U^+ = 0.1$ and -0.1, respectively. Comparison between the positive

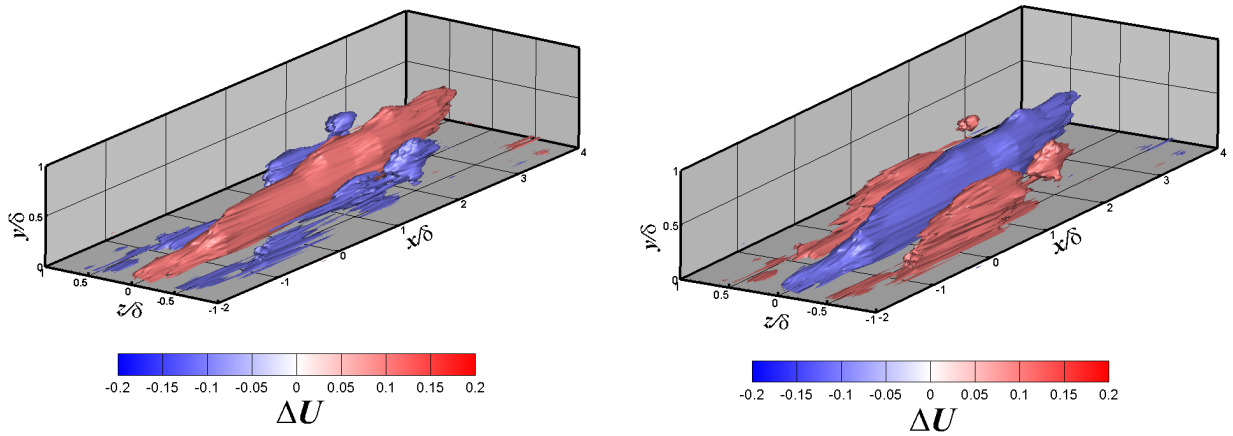

Figure 6: Volumetric reconstruction using interpolation between each PIV data plane of a) $\Delta U_h^+(x,y,z)$ (conditioned on $\tau(t=0)>0$), and b) $\Delta U_l^+(x,y,z)$ (conditioned on $\tau(t=0)<0$.

and negative conditions shows that the flanking oppositely-signed regions to the central correlated region is slightly upstream about δ for the negative shear condition compared to the positive. They also appear to be larger, and extend further away from the wall. Each conditional average has striking similarity to the cross correlation volume of Fig. 5, with opposite sign for the negative condition. Once again, the slight asymmetries in the spanwise direction for each condition supports the high quality of the experiments.

With recent works investigating the impact of wall-attached structures on the boundary layer, such as through the self-similarity of the linear coherence spectrum (Baars et al. (2017); Pabon et al. (2018); Baidya et al. (2019)), a conditional sampling scheme was developed to identify the pattern these structures create. From previous work in the current setup using hot-wire anemometry in Pabon et al. (2018), an approximate linear relation region in the coherence spectrum has been identified within $2<\lambda_\infty/\delta<10$, where $\lambda_\infty = U_\infty/f$ since only temporal measurements are taken. To isolate velocity dynamics in this region, a bandpass filter is applied to the wall shear stress with these limits. Conditions on this filtered mean subtracted wall shear stress signal, $\tilde{\tau}'$, are further divided into four regions: I) locally high positive shear stress with low gradient magnitude, II) locally high negative shear stress with low gradient magnitude, III) locally high positive gradient with low magnitude of shear, and IV) locally high negative gradient with low magnitude of shear stress. The time gradient of the bandpassed signal is calculated using a first-order backward finite difference, for simplicity as well as being for future real time control applications, calculated as $\partial\widetilde{\tau}_w'(t_k) = \widetilde{\tau}_w'(t_k) - \widetilde{\tau}_w'(t_{k-1})$. A representation of these regions can be seen in a simple schematic in Fig. 7. These differential level VITA conditions, henceforth referred to as DIFFLEVITA, are

$$\text{DIFFLEVITA } I = \quad \text{VITA}(\widetilde{\tau}_w') > C_I\sigma_{\tilde{\tau}} \quad \cap \quad |\text{VITA}(\partial\widetilde{\tau}_w')| < D_I\sigma_{\partial\tilde{\tau}} \tag{5}$$

$$\text{DIFFLEVITA } II = \quad \text{VITA}(\widetilde{\tau}_w') < -C_{II}\sigma_{\tilde{\tau}} \quad \cap \quad |\text{VITA}(\partial\widetilde{\tau}_w')| < D_{II}\sigma_{\partial\tilde{\tau}} \tag{6}$$

$$\text{DIFFLEVITA } III = \quad \text{VITA}(\partial\widetilde{\tau}_w') > C_{III}\sigma_{\partial\tilde{\tau}} \quad \cap \quad |\text{VITA}(\widetilde{\tau}_w')| < D_{III}\sigma_{\tilde{\tau}} \tag{7}$$

$$\text{DIFFLEVITA } IV = \quad \text{VITA}(\partial\widetilde{\tau}_w') < -C_{IV}\sigma_{\partial\tilde{\tau}} \quad \cap \quad |\text{VITA}(\widetilde{\tau}_w')| < D_{IV}\sigma_{\tilde{\tau}} \tag{8}$$

and the coefficients C and D are threshold coefficients for the signal magintude and differential signal magnitude, respectively. The additional threshold value for each signal increases arbitrariness for a one-to-one comparison, but even for the classic VARVITA condition, there is no threshold value at which the result is independent of threshold Morrison et al. (1989). As such, only qualitative conclusions at best can be taken, and no large weight can be placed on actual magnitudes from the conditional analysis. The resulting thresholds, to be rooted in a physical phenomenon related to the wall-attached and relevant scales, are chosen such that the total number of samples retained for each condition is 9% of the total, half the traditional bursting frequency (Corino and Brodkey (1969)). In addition, the thresholds were desired to be symmetric between the positive and negative conditions, such that the final threshold values were $C_I = C_{II} = C_{III} = C_{IV} = 0.75$ and $D_I = D_{II} = D_{III} = D_{IV} = 0.5$.

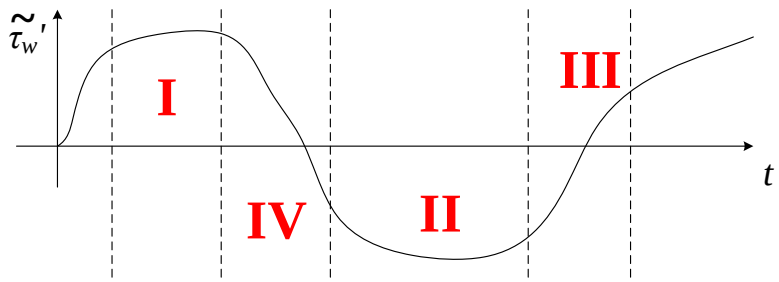

Figure 7: Schematic showing representative bandpassed wall shear stress signal, identifying regions that satisfy DIFFLEVITA conditions I-IV.

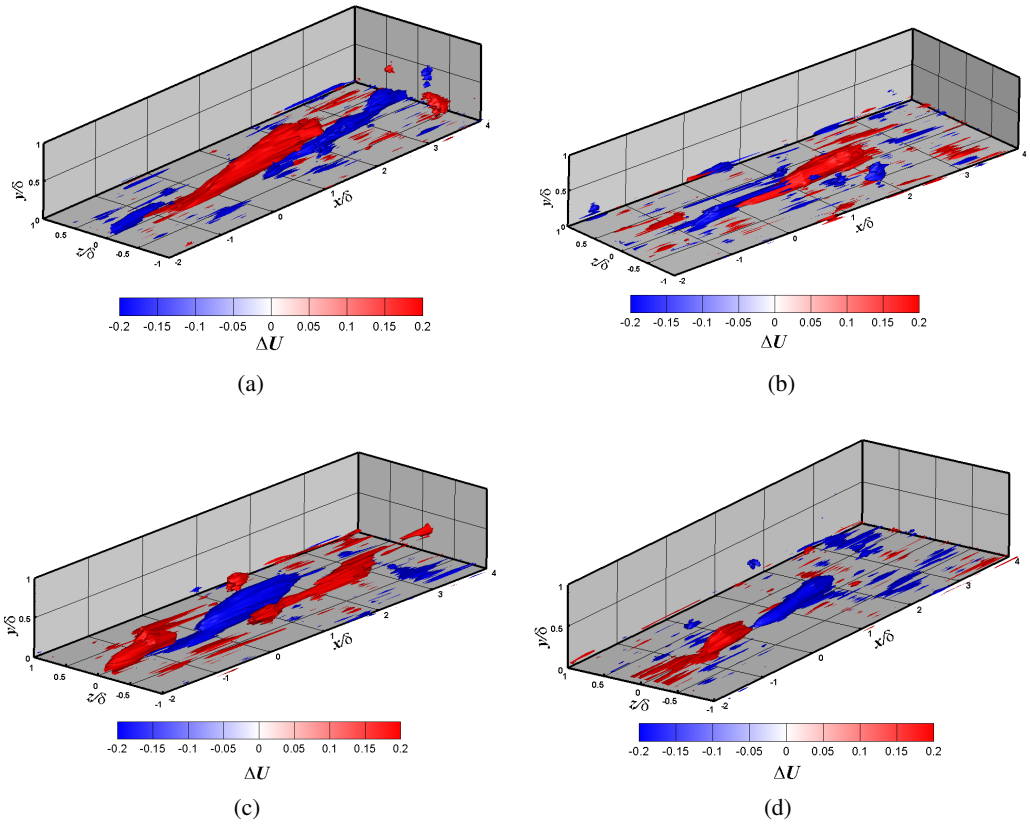

Figure 8: Volumetric reconstruction using interpolation between each PIV data plane of difference between conditionally averaged streamwise velocity field and mean streamwise velocity field given a) DIFFLEVITA I, b) DIFFLEVITA IV, c) DIFFLEVITA II, and d) DIFFLEVITA III. Note the increased isosurface values of 0.2 and -0.2, respectively,

Isosurfaces of the volumetric reconstruction of each condition is shown in Fig. 8, in the order *I*, *IV*, *II*, and *III*, suggested by the periodic schematic in 7. Each spatial representation presents as a phase of a periodic structure that convects downstream following the phase pattern, as well as diminishes at distance to the sensor. Within the field of view, streamwise gradients are visible using this conditional average. This

implies that a life-cycle duration of wall attached eddies is captured here at a single point of wall shear stress, with the conditional procedure selecting structures of streamwise wavelength of approximately 4δ. These present as inclined structures that follow each other in convection. The older, convected, and oppositely signed structure is influencing the lift-up and inclination of the newer one. This highlights potential wavelengths and structure models to target for future flow control experiments.

4 Conclusions

The use of MEMS floating element wall shear stress sensors in a turbulent boundary layer with simultaneous PIV was completed for the first time in this study. A suitable experimental procedure is described that limited the sensor to damage from seed-exposure as well as data corruption from laser radiation. Multiple, discrete experiments moving the PIV measurement plane allows for a volumetric reconstruction of the cross correlation, as well as conditional averages on the wall shear stress. High PIV-wall shear stress correlation values imply correlation based estimation techniques have merit in following the experimental procedures, with spectral techniques possible, but limited due to the dissimilar sampling rate, with higher capture rate PIV being suggested. The large number of PIV image pairs used in the study ($\approx 100,000$) helps acquire both extreme, rare events of interest to turbulence production, as well as ensuring convergence of statistics. A novel differential and level based conditional sampling scheme is introduced to capture a periodic structure associated with wall-attached scaling. The investigation of the dynamic component of identified shear events in this work is intended to continue and develop drag control methodologies and structure identification.

Acknowledgements

This material is based upon work supported by the National Science Foundation Graduate Research Fellowship under Grant No. DGE-1315138. The authors also wish to acknowledge the support of the Florida Center for Advanced Aero-Propulsion (FCAAP).

References

Baars WJ, Hutchins N, and Marusic I (2017) Self-similarity of wall-attached turbulence in boundary layers. *Journal of Fluid Mechanics* 823:R2

Baidya R, Baars WJ, Zimmerman S, Samie M, Hearst RJ, Dogan E, Mascotelli L, Zheng X, Bellani G, Talamelli A, Ganapathisubramani B, Hutchins N, Marusic I, Klewicki J, and Monty JP (2019) Simultaneous skin friction and velocity measurements in high Reynolds number pipe and boundary layer flows. *Journal of Fluid Mechanics* 871:377–400

Blackwelder RF and Kaplan RE (1976) On the wall structure of the turbulent boundary layer. *Journal of Fluid Mechanics* 76:89–112

Blackwelder RF and Kovasznay LSG (1972) Time Scales and Correlations in a Turbulent Boundary Layer. *Physics of Fluids* 15:1545–1554

Corino ER and Brodkey RS (1969) A visual investigation of the wall region in turbulent flow. *Journal of Fluid Mechanics* 37:1

Hanson RE, Buckley HP, and Lavoie P (2012) Aerodynamic optimization of the flat-plate leading edge for experimental studies of laminar and transitional boundary layers. *Experiments in Fluids* 53:863–871

Kovasznay LS, Kibens V, and Blackwelder RF (1970) Large-scale motion in the intermittent region of a turbulent boundary layer

LaVision (2016) FlowMaster. Technical report. LaVision GmbH. Gottingen, Germany

Mills DA, Barnard C, and Sheplak M (2017) Characterization of a Hydraulically Smooth Wall Shear Stress Sensor for Low-Speed Wind Tunnel Applications. in *55th AIAA Aerospace Sciences Meeting*. American Institute of Aeronautics and Astronautics, Grapevine, TX

Mills DA, Patterson WC, Keane C, and Sheplak M (2018) Characterization of a Fully-Differential Capacitive Wall Shear Stress Sensor for Low-Speed Wind Tunnels. *2018 AIAA Aerospace Sciences Meeting* pages 1–14

Morrison JF, Tsai HM, and Bradshaw P (1989) Conditional-sampling schemes for turbulent flow, based on the variable-interval time averagins (VITA) algorithm. *Experiments in Fluids* 7:173–189

Naughton JW and Sheplak M (2002) Modern developments in shear-stress measurement. *Progress in Aerospace Sciences* 38:515–570

Nogueira J, Lecuona A, and Rodríguez PA (1997) Data validation, false vectors correction and derived magnitudes calculation on PIV data. *Measurement Science and Technology* 8:1493–1501

Pabon RJ (2018) *Experimental studies of organized motions in a turbulent boundary layer and their imprint on wall shear stress*. Ph.D. thesis. University of Florida

Pabon RJ, Ukeiley L, Sheplak M, and Barnard Keane C (2018) Characteristics of turbulent boundary layer large scale motions using direct fluctuating wall shear stress measurements. *Physical Review Fluids* 3:114604

Raffel M, Willert CE, Wereley S, and Kompenhans J (2007) *Particle Image Velocimetry*. Springer Berlin Heidelberg, Berlin. second edi edition

Wallace JM, Eckelmann H, and Brodkey RS (1972) The wall region in turbulent shear flow. *Journal of Fluid Mechanics* 54:39

Westerweel J, Fukushima C, Pedersen JM, and Hunt JCR (2005) Mechanics of the turbulent-nonturbulent interface of a jet. *Physical Review Letters* 95:199–230

Zhou J, Adrian RJ, Balachandar S, and Kendall TM (1999) Mechanisms for generating coherent packets of hairpin vortices in channel flow. *Journal of Fluid Mechanics* 387:353–396